CrossMark

Evaluating Weather Research and Forecasting Model Sensitivity to Land and Soil Conditions Representative of Karst Landscapes

Christopher M. Johnson[1,2] · Xingang Fan[1] ·
Rezaul Mahmood[1,2] · Chris Groves[1,3] · Jason S. Polk[1,4] ·
Jun Yan[1]

Abstract Due to their particular physiographic, geomorphic, soil cover, and complex surface-subsurface hydrologic conditions, karst regions produce distinct land–atmosphere interactions. It has been found that floods and droughts over karst regions can be more pronounced than those in non-karst regions following a given rainfall event. Five convective weather events are simulated using the Weather Research and Forecasting model to explore the potential impacts of land-surface conditions on weather simulations over karst regions. Since no existing weather or climate model has the ability to represent karst landscapes, simulation experiments in this exploratory study consist of a control (default land-cover/soil types) and three land-surface conditions, including barren ground, forest, and sandy soils over the karst areas, which mimic certain karst characteristics. Results from sensitivity experiments are compared with the control simulation, as well as with the National Centers for Environmental Prediction multi-sensor precipitation analysis Stage-IV data, and near-surface atmospheric observations. Mesoscale features of surface energy partition, surface water and energy exchange, the resulting surface-air temperature and humidity, and low-level instability and convective energy are analyzed to investigate the potential land-surface impact on weather over karst regions. We conclude that: (1) barren ground used over karst regions has a pronounced effect on the overall simulation of precipitation. Barren ground provides the overall lowest root-mean-square errors and bias scores in precipitation over the peak-rain periods. Contingency table-based equitable threat and frequency bias scores suggest that the barren and forest experiments are more successful in simulating light to moderate rainfall. Variables dependent on local surface conditions show stronger contrasts between karst and non-karst

✉ Xingang Fan
   xingang.fan@wku.edu

[1] Department of Geography and Geology, Western Kentucky University, Bowling Green, KY 42101, USA

[2] Kentucky Climate Center, Western Kentucky University, Bowling Green, KY 42101, USA

[3] Crawford Hydrology Laboratory, Western Kentucky University, Bowling Green, KY 42101, USA

[4] Center for Human GeoEnvironmental Studies, Western Kentucky University, Bowling Green, KY 42101, USA

regions than variables dominated by large-scale synoptic systems; (2) significant sensitivity responses are found over the karst regions, including pronounced warming and cooling effects on the near-surface atmosphere from barren and forested land cover, respectively; (3) the barren ground in the karst regions provides conditions favourable for convective development under certain conditions. Therefore, it is suggested that karst and non-karst landscapes should be distinguished, and their physical processes should be considered for future model development.

1 Introduction

Karst terrain covers approximately 20% of the Earth's ice-free land surface, with an estimated 40% of the USA east of Tulsa, Oklahoma comprising karst landscapes (White et al. 1995; Ford and Williams 2007) as shown in Fig. 1a. Physical conditions associated with well-developed karst landscapes may affect local and regional weather systems through various processes related to land–atmosphere interactions (Jiang and Yuan 1999; Leeper et al. 2011; Durkee et al. 2012). Karst is defined as a type of terrain, generally underlain by soluble carbonate rocks such as limestone or dolomite, where the topography is primarily formed by the dissolution of rock, and which may be characterized by sinkholes, sinking streams, closed depressions, subterranean drainage, and caves (White 1988; Ford and Williams 2007). Most often, karst landscapes form highly permeable aquifer systems within the carbonate bedrock, which typically have a thin soil cover, if any, and are able to support a variety of surface-land cover ranging from bare, stony rock surfaces to vegetation ranging from cacti to dense tropical forests, depending on the climate and latitude. The water table may be
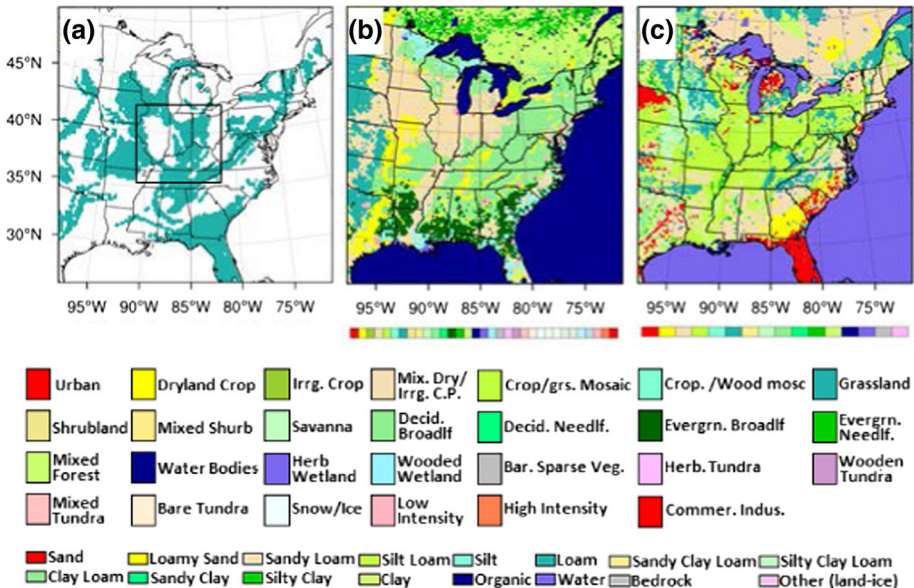

Fig. 1 Study area: **a** two nested model domains with colour shades representing the areas of karst landscapes; **b** land-cover types based on data from the 2006 National Land Cover Database; **c** soil types

tens to hundreds of metres below the surface, depending on the topography, and the land surface is sometimes rugged and heavily weathered. Soil productivity can be limited by the low nutrient and water availability and the steep, sloping terrain (Li et al. 2003; Ford and Williams 2007; Palmer 2007). Generally, rainfall reaching the ground of most landscapes evaporates, infiltrates, or moves laterally at or near the surface as runoff or interflow. However, on well-developed karst topography, there is often limited surface runoff, since most or all of the precipitation rapidly infiltrates directly into the karst aquifer, either through the soil or sinking streams (Crowther 1987; Hess and White 1989; Groves and Meiman 2005; Groves 2007; Leeper et al. 2011). Groves et al. (2005) were able to capture surface rainfall in a cave within 30–45 min of observed precipitation, showing a clear indication of the rapid transport of meteoric recharge into karst aquifers. Milanovic (1981) observed that karst groundwater tables vary by as much as 100 m after a rain event, which may cause localized flooding and the increase in atmospheric moisture availability within the root zone. Furthermore, gradients in soil moisture may lead to differential heating at the surface through evaporative cooling, thus promoting the development of mesoscale circulations (Milanovic 1981). Karst landscapes and their geomorphic and hydrologic characteristics may well influence the land–atmosphere interface differently when compared with non-karst areas (White et al. 1995; Jiang and Yuan 1999; Bonacci et al. 2009; Heilman et al. 2009; Leeper et al. 2011).

Surface and sub-surface karst features, such as sinkholes, underground drainage systems, vertical shafts, and springs, significantly influence localized drainage patterns and hydrological processes. Karst topography, through its effect on local hydrology, can, in turn, significantly alter soil-moisture distributions, which may induce important feedbacks between karst regions and the near-surface atmosphere (Leeper et al. 2011). There is very limited research on the direct impact of karst landscapes on climate, or the attribution of weather/climate events to karst systems. Ji et al. (2015) studied the increasing trend of flood and drought disasters in the past 500 years over a well-developed karst region in south-west China, and found that, under the climate change regimes and human activities investigated, the karst region is susceptible to more frequent flooding and drought due to its land-surface geomorphology. Zhang et al. (2010) analyzed extreme precipitation distributions in another karst region in Guizhou, China, and also noticed an increasing trend of extreme events. However, it is well-known that spatial and temporal heterogeneity in both soil-moisture distributions and wet–dry transitions promote localized mesoscale circulations and subsequent convection (Clark and Arritt 1995; McPherson 2007). Furthermore, Leeper et al. (2011) conducted a sensitivity study for precipitation over karst landscapes in Kentucky and showed that, even under moderate synoptic forcing, adjacent wet/dry land-surface conditions can modify energy balances, the evolution of the planetary boundary layer, mesoscale circulations, and the locations of convection. A study of the 1–2 May 2010 historic mid-south flood suggests that the heaviest localized precipitation fell over the areas located along or adjacent to well-developed karst hydrological boundaries (Durkee et al. 2012).

The complexity of karst groundwater flow systems is such that, while karst hydrological modelling has progressed, many challenges still exist (e.g., Meng and Wang 2010; Hartmann et al. 2013). While quantitative descriptions of land-surface conditions and processes coupled with atmospheric models also continue to evolve, none have proper representations of karst landscapes (Chen and Dudhia 2001; Dai et al. 2003; Skamarock et al. 2008). Limited research has been completed on the direct impacts of karst landscapes on atmospheric processes and karst–atmosphere coupling. However, with the vast improvement in computational resources and the ability to understand and better simulate these processes at much higher rates and resolutions, studying the impacts of localized karst features has become increasingly feasible. Prior to representing karst-landscape characteristics in land-surface models or the coupling

of karst conditions with atmospheric processes, exploratory methods, such as sensitivity experiments, facilitate the investigation of the potential effects of karst landscapes on the atmosphere. Fan (2009) used the Weather Research and Forecasting (WRF) model to study the impacts of changes on regional weather simulations by surface-heating conditions derived from soil-temperature observations. They indicate that incorporation of the observed soil temperatures introduces a persistent soil heating that is favourable to convective development and, consequently, the improved simulation of precipitation. Gao et al. (2013) used the WRF model, which is coupled with the simplified Simple Biosphere Model of Xue et al. (1991), to study the impacts of land degradation over the Guizhou karst plateau on the regional climate. The degraded lands were represented by short shrubs with bare soil for moderately degraded land or bare soil for severely degraded land, with the degraded land over the south-west China karst region shown to have an impact on the regional climate. We use a similar approach to Fan (2009) and Gao et al. (2013) to simulate the responses of the WRF model to different land-cover and soil types over the karst regions of central USA shown in Fig. 1. If the area of a cell is dominated by karst, it is considered as a karst region, which is similar to the treatment of land use and soil types in the WRF modelling system (Chen and Dudhia 2001; Chen et al. 2007; Skamarock et al. 2008).

Our objective is to explore whether weather events are sensitive to the land-surface conditions available in the current WRF model, whether the model can mimic certain characteristics of karst landscapes, and whether the model is able to distinguish between the input conditions defining karst and non-karst conditions. Given that no existing model distinguishes between karst and non-karst conditions, the experiments are designed to determine if any existing land types in the model, along with their physical parameters, result in improved weather simulations in karst regions, and thereby serving as a "proof-of-concept" before investment in additional effort to develop more realistic physical and/or chemical processes of karst regions. As it is an exploratory sensitivity study, the experiments reflect only some of those characteristics representative of a karst landscape.

Additional objectives examine how the proposed land-cover or soil types may mimic karst impacts. As with many karst landscapes, the study area (Fig. 1) is characterized by an uneven soil-bedrock interface buried under a typically shallow layer of soil and/or fully exposed bedrock with no soil cover. In the case of the exposed karst (i.e., exposed bare rock surfaces), there is higher albedo, higher runoff, and less soil moisture than for soil-covered areas. The "barren" land-cover type in existing land-surface models is sparsely vegetated, and thus an approximation of exposed karst areas. This type of land cover typically leads to a higher sensible heat flux, higher air and surface temperatures, and lower soil moisture. Forest land cover is used as a contrasting experiment, where forested land cover over a karst region may reduce albedo, increase evapotranspiration, and, therefore, increase moisture transfer into the atmosphere (Bonan 2008). While not yet investigated for karst areas, deeper root systems of the forest over a karst landscape help preserve soil moisture by penetrating into bedrock fractures, which may lead to possible impacts on atmospheric conditions (e.g., Jackson et al. 1999; Schwinning 2008).

As indicated earlier, an important feature of karst is the existence of highly permeable bedrock, resulting in the rapid drainage of rainwater into the subsurface, whose representation may be the prescription of sandy soils in the existing land-surface model, which have the lowest moisture content and relatively high permeability (Mitchell 2005). The sensitivities of five selected weather events to the karst landscape are tested with each of the representations mentioned above using the Advanced Research WRF model version 3.2.1 (Skamarock et al. 2008). Brief descriptions for the weather events and detailed experimental designs are given

in Sect. 2, Sect. 3 presents the analysis and discussion of model simulations, with concluding remarks summarized in Sect 4.

2 Model, Data, and Experimental Design

The national karst map from the U.S. Geological Survey (Davies et al. 1984; Weary and Doctor 2014) was incorporated into the WRF model, which is configured here with two one-way nested domains (Fig. 1a). The model resolution for the outer domain is 18 km (covering 2700 km east to west; north to south) and 6 km for the nested domain (extending 906 km east to west; north to south), with 49 vertical Eta levels extending from the surface to 100 hPa (here, Eta levels refers to a vertical coordinate system based on normalized pressures above mean sea level, Mesinger and Janjic 1974). Model physical parametrizations follow Gaines (2012), where a squall-line event in central USA was simulated with various combinations of parametrizations, including the Lin microphysical parametrization (Lin et al. 1983), the Kain-Fritsch (new Eta) cumulus parametrization over both domains (Kain and Fritsch 1993), the ACM2 (Pleim) planetary boundary-layer parametrization (Skamarock et al. 2008), the Rapid Radiative Transfer Model longwave radiation parametrization (Mlawer et al. 1997), the Goddard shortwave radiation parametrization (Chou et al. 1998), and the Noah land-surface model (Chen and Dudhia 2001). Model simulations are driven by North American Regional Reanalysis data (Mesinger et al. 2006).

As noted previously, five convective weather events over the karst region were selected for the sensitivity study (Table 1), featuring a wide variety of total precipitation from light to moderate rainfall, to a historic flooding event (Fig. 2). The selection of convective events facilitates consideration for any initial feedback from the karst landscape to the atmosphere under various conditions, such as three different seasons, including late spring, early summer, and autumn, and which represent typical atmospheric conditions for the study area.

Considered are a stationary front due to downstream blocking near the eastern Atlantic Ocean (case 1), a cold front becoming stationary over the Ohio Valley region (case 2), a weakly forced summertime cold front (case 3), a mesoscale convective system (case 4), and a strong cold front that produced record rainfall across the Ohio and Tennessee Valley regions (case 5), for a total of 20 simulations (five weather events and four land-cover scenarios as described below). Light to moderate rainfall amounts were recorded during the stationary front (case 1) and the weak cold front (case 3), with larger amounts produced from the two cold fronts (cases 2 and 5) and the mesoscale convective system (case 4). We have previously investigated these precipitation events, for which we have developed comprehensive knowledge (e.g., Quintanar et al. 2008, 2009; Durkee et al. 2012; Quintanar and Mahmood 2012; Suarez et al. 2014).

Table 1 Simulation and analysis time periods of the five chosen cases with analysis and rainy periods

Case	Simulation Time (HHMM dd-mm-yyyy)	Analysis[a] (h)			Rain Day (HHMM dd-mm)
1	2100 10-06-2006 – 0000 13-06-2006	3	24	24	0000 11-06 – 0000 12-06
2	2100 16-06-2006 – 0000 19-06-2006	3	24	24	0000 18-06 – 0000 19-06
3	2100 22-06-2006 – 0000 25-06-2006	3	24	24	0000 23-06 – 0000 24-06
4	2100 28-09-2008 – 0000 01-10-2008	3	12 24 12		1200 29-09 – 1200 30-09
5	2100 30-04-2010 – 0000 03-05-2010	3	48		0000 01-05 – 0000 03-05

All times are shown in UTC unless indicated (e.g., where local times are used below)

[a] The 51-h simulation timeline shows a 3-h spin-up (light grey), model simulation (grey), and analysis period (hatched) corresponding to the peak rain-day period
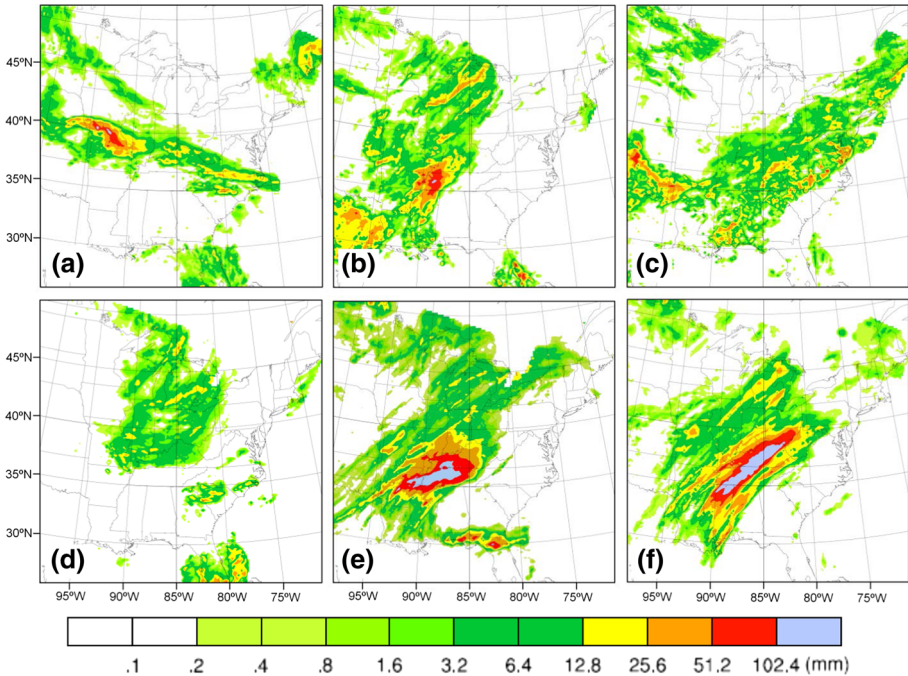
Fig. 2 The 24-h accumulated Stage-IV precipitation (mm) ending at: **a** case 1: 0000 UTC 12-06-2006; **b** case 2: 0000 UTC 19-06-2006; **c** case 3: 0000 UTC 24-06-2006; **d** case 4: 1200 UTC 30-09-2008; **e** case 5: day 1 0000 UTC 02-05-2010; and **f** case 5: day 2 0000 UTC 03-05-2010

The land cover of the outer domain shown in Fig. 1b is based on the 2006 National Land Cover Dataset (Fry et al. 2011), and depicts a small band of the dryland crop and pasture located over the Ohio and Tennessee Valley regions, with a small area extending through central Kentucky, Tennessee, and southwards. Largely deciduous broadleaf forest surrounds the small area of dryland crop and pasture within the nested domain. Areas along the Mississippi River and northwards near the Ohio River mainly consist of mixed dryland/irrigated crop and pasture.

The experiments consist of control, barren-land, forest, and sandy-soil simulations for each event, with specific land and soil types used in the corresponding model experiment to best represent a karst landscape over the karst areas (Fig. 1a), and to study the potential atmospheric impacts. The control run uses the WRF model with the default land cover and soil types as shown in Fig. 1b, c. The barren experiment is conducted by changing all land-cover types over the karst areas (Fig. 1a) to a barren-land type, with little or no vegetation cover to better simulate karst landscapes of this variety. For the forest experiment, all land-cover types over the karst areas are changed to forest. Another change introduced to both the barren and forest experiments, is to the vegetation fraction over karst areas, which is changed to 0 and 100%, respectively, corresponding to the land-cover types. The last experiment places sandy soils over the karst areas (Fig. 1a), but with the same land-cover types as the control experiment. This simulates the rapid drainage of water, which is associated with dry sands and may reflect karst hydrological characteristics with high bedrock permeability. As sand has the least water content among all of the soil types in the current Noah land-surface model (Mitchell 2005), it was chosen for this experiment.

The numerical experiments are initiated with a 3-h spin-up, which allows the model to adjust to its background forcing, and are followed by a simulation of 48-h duration (see Table 1). The results of 24-h simulation periods (the hatched grey areas in Table 1) are analyzed and verified, corresponding to the rainy period for each case, and allowing sufficient time for changes in land cover and soils to take effect. The rainy period was set immediately after model spin-up in cases 1, 3 and 5, case 4 allowed for a further 12 h, and case 2 allowed for 24 h between spin-up and the rainy period. Case 5 is analyzed for a longer period of time (two 24-h analysis periods) to more accurately reflect the longevity of the convective event, which produced periods of heavy rain over the Tennessee and Ohio Valley regions.

The model-simulated precipitation is compared with the National Centers for Environmental Prediction (NCEP) multi-sensor precipitation analysis Stage-IV dataset, which is based on a combination of quality controlled radar and gauge observations (Lin 2011). Each of the experiments is also compared with the control run for the sensitivity analysis. Model evaluations are performed using statistical scores, including the root-mean-square error ($RMSE$) and bias ($BIAS$) using the NCEP Automated Data Processing Global Upper Air and Surface Weather Observations (May 1997—continuing, available at http://rda.ucar.edu/datasets/ds337.0/, accessed October 2015). While the $RMSE$ measures the overall error of a simulated variable compared with its observations, the bias assesses the systematic underestimation ($BIAS < 0$) or overestimation ($BIAS > 0$), with $BIAS = 0$ being perfect. For precipitation, the 2×2 contingency table-based equitable threat score (ETS) and frequency bias score ($fBIAS$) are calculated for a variety of thresholds for comparison (Wilks 2010), with ETS values considered in assessing the model skill of precipitation simulations. Higher ETS values represent more accurate results (termed more "skilful", with $ETS = 1$ being perfect) and lower values represent the opposite. The related $fBIAS$ score represents the bias of frequency of a particular rain amount (used as a threshold) or greater, where $fBIAS = 1$ represents a perfect skill, while $fBIAS > 1$ (or < 1) indicates overestimation (or underestimation) of the frequency of the given precipitation threshold or greater. Other model-simulated and derived variables, such as the convective available potential energy ($CAPE$, energy available to an ascending air parcel), convective inhibition (CIN, energy needed to lift an air parcel to its level of free convection), temperature, dew point temperature, equivalent potential temperature, and surface heat fluxes are used in analyzing the mesoscale convective development.

3 Model Simulation Analysis

The results of model simulations are compared with observations, (1) to evaluate their performance; and (2) to investigate the impacts of the different land-cover and soil conditions over karst regions during the five chosen precipitation events. Case 4 is presented here in detail with a focus on the nested domain, with general results presented from the other cases. Case 4 is a mesoscale convective system, where moderate lift, moisture, instability, and favourable vertical wind shear contribute to its substantial growth.

3.1 Model Verification

3.1.1 Precipitation

The 24-h accumulated precipitation of case 4 from the control simulation during the rainy period (1200 UTC 29-09-2008 to 1200 UTC 30-09-2008) is shown in Fig. 3a for the nested domain, where the major precipitation areas are simulated well, with light to moderate
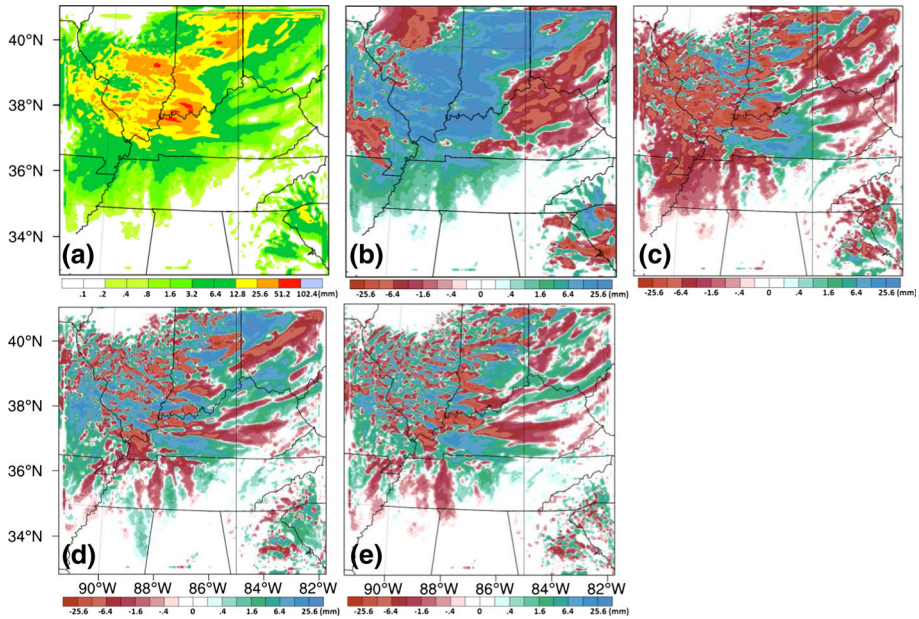
Fig. 3 The 24-h accumulated precipitation (mm) and differences (mm) for case 4 over the nested domain, and ending at 1200 UTC 30-09-2008: **a** control run; **b** difference between control and Stage-IV data as shown in Fig. 2d; **c** difference between barren and control simulations; **d** difference between forest and control simulations; **e** difference between sandy-soil and control simulations

amounts of rainfall of 0.2–51.2 mm over the domain. Larger amounts of rainfall are found over the western portions of Kentucky and into south Illinois and Indiana. Figure 3b shows the difference in 24-h accumulated precipitation between the control simulation and Stage-IV data. For most areas receiving precipitation, especially locations along west Kentucky and south Indiana and Illinois, a large area of positive difference (control minus Stage-IV data) in precipitation is detected, which is particularly noticeable over areas with the heaviest rainfall, indicating a positive bias in the simulation. In contrast, the model produces a negative bias over areas of lighter precipitation.

Barren – control (i.e. subtracting control results from the barren results) simulations show a negative bias of precipitation over areas with the heaviest amounts of rainfall (Fig. 3c), suggesting the barren experiment corrects some of the overestimation of the control run for heavy rainfall. This finding also somewhat concurs with Leeper et al. (2011), where a lowering of the soil moisture in the model (thereby simulating the lower karst soil moisture) produces precipitation in better agreement with the observations. The barren experiment shows large positive differences (6.4–25.6 mm) in light to moderate precipitation areas along the western Kentucky region where the control simulation underestimates the precipitation. Hence, using the barren-land type to simulate a karst landscape improves the precipitation estimates, which also holds true for the other cases, as discussed below.

For the forest experiment (Fig. 3d), differences in 24-h rainfall compared with the control experiment are more spatially intermittent than, for example, the control differences with the Stage-IV data (Fig. 3b). Larger areas of positive differences are evident across Kentucky and into south Indiana/Illinois. Results from the west Kentucky and Missouri karst regions reveal areas of positive total precipitation differences where the precipitation is light to
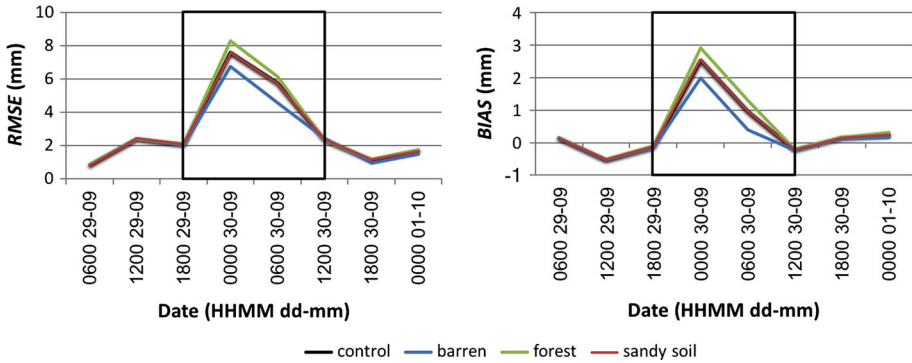
Fig. 4 Values of *RMSE* and *BIAS* of 6-h accumulated precipitation from the control, barren, forest, and sandy-soil experiments for case 4, verified with Stage-IV precipitation data. The dates shown represent the ending point of each 6-h period

moderate (Fig. 3a, d). While the precipitation differences between the sandy-soil and control runs (Fig. 3e) are broadly similar to those from the forest experiment, the sandy-soil-control comparison shows smaller magnitudes in the total rainfall differences, especially with smaller positive differences, than for the forest-control comparison.

To better understand the model performance, a further quantitative analysis of precipitation is conducted to numerically differentiate among the land-cover and soil types, where the analysis of *RMSE* and *BIAS* values provides a better assessment of the accuracy of the simulations.

The *RMSE* and *BIAS* values of model-simulated 6-h precipitation for case 4 are compared with the Stage-IV precipitation for the eight 6-h periods after the 3-h spin-up time in Fig. 4, where the barren simulation performs better than the other experiments. Of the eight 6-h periods, the barren experiment shows the largest improvements over the four time periods according to *RMSE* and *BIAS* values (Fig. 4), all of which correspond to the rainy period, while the remaining four time periods (ending at 0600, 1200 UTC 29-09-2008, 1800 UTC 30-09-2008 and 0000 UTC on 01-10-2008) show minimal differences from the other two experiments. Furthermore, the averaged *RMSE* and *BIAS* values over all eight time periods indicate that the barren simulation has the lowest *RMSE* (2.69 mm) and the least absolute *BIAS* (0.24 mm). The forest simulation has the highest average *RMSE* (3.14 mm) and *BIAS* (0.51 mm) values. The sandy-soil *RMSE* (2.95 mm) and *BIAS* (0.41 mm) values show no notable change from the control run (*RMSE* = 2.98 mm; *BIAS* = 0.40 mm), as both remain in between the estimates for the barren and forest simulations. These results suggest that the approximation of karst landscapes as barren land produces the best simulation of precipitation. The change from the original land-cover types (the control run) to forest is less dramatic and produces more uncertainty in the simulation. The smaller differences between the sandy-soil and control runs than those between the barren and control runs imply that the soil type plays a lesser role than the land-cover type on the simulation of precipitation (the soil types in the barren experiment and the land-cover types in sandy-soil experiment are the same as for the control experiment).

After evaluating both the *RMSE* and *BIAS* values, which show overall differences of model-simulated precipitation from the observations, the evaluation of *ETS* and *fBIAS* values is also performed to clarify the extent to which each simulation experiment accurately simulates the precipitation amount. The *ETS* and *fBIAS* values are calculated for eight precipitation
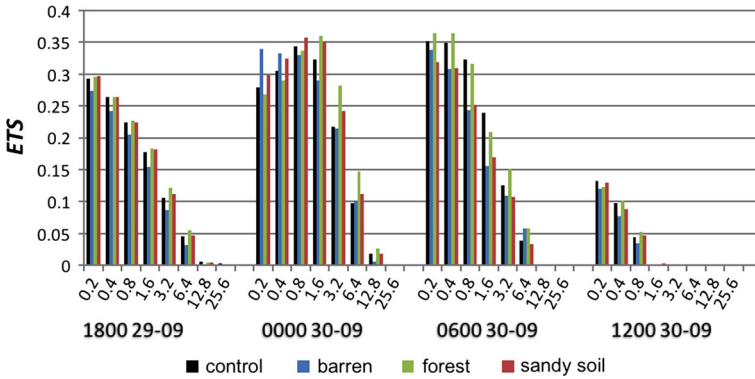
Fig. 5 Equitable threat score for eight precipitation levels (0.2, 0.4, 0.8, 1.6, 3.2, 6.4, 12.8, 25.6 mm) during the 1800 UTC 29 September 2008–1200 UTC 30 September 2008 rainy period for the control, barren, forest and sandy-soil experiments of case 4
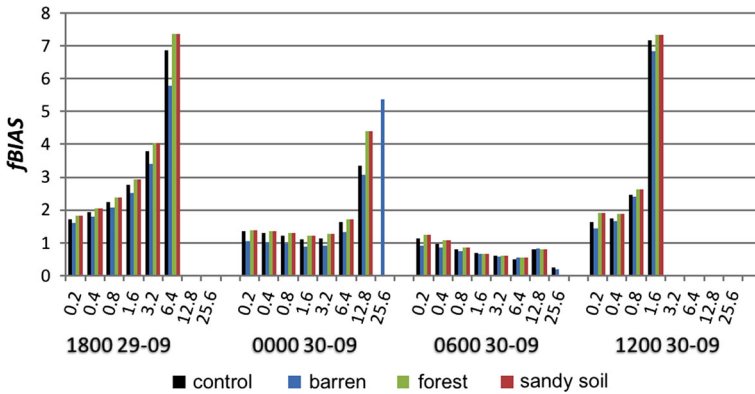

Fig. 6 Frequency bias score for eight precipitation levels (0.2, 0.4, 0.8, 1.6, 3.2, 6.4, 12.8, 25.6 mm) during the 1800 UTC 29 September 2008–1200 UTC 30 September 2008 rainy period for the control, barren, forest and sandy-soil experiments of case 4

thresholds (i.e. 0.2, 0.4, 0.8, 1.6, 3.2, 6.4, 12.8 and 25.6 mm). Further evaluation focuses on the four 6-h periods during the rainy period (1200 UTC 29 September 2008–1200 UTC 30 September 2008) for case 4 as suggested by the *RMSE* and *BIAS* values. The *ETS* values give the highest magnitudes during these four time periods (Fig. 5, other times with lower *ETS* values not shown) along with the overall lowest *fBIAS* values, which are also closest to unity (Fig. 6, other times with worse *fBIAS* values not shown). These results suggest that the model performs well for smaller precipitation levels of 0.2–1.6 mm (Figs. 5, 6). It is important to note that during these time intervals for case 4, the *ETS* values increase during the middle of the rainy period, while the *fBIAS* values are more dramatically reduced. The lower *fBIAS* values are considered an improvement among the model simulations, suggesting the model satisfactorily simulates the precipitation during this period.

Among the experiments for all the cases, the average *ETS* and *fBIAS* values are calculated to further examine model skill and accuracy. Figure 7 presents the averaged *ETS* and *fBIAS* values for cases 1, 2, 3 and 5 for the eight precipitation thresholds through each rainy period as defined in Table 1, revealing model simulations with improved skill and accuracy for all cases
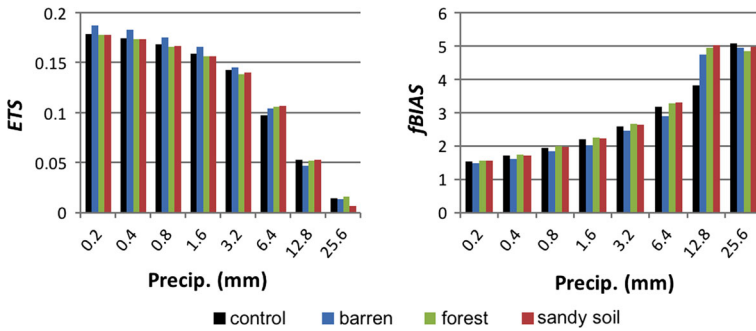
Fig. 7 Averaged *ETS* and *fBIAS* values for eight precipitation levels (0.2, 0.4, 0.8, 1.6, 3.2, 6.4, 12.8, 25.6 mm) during rainy periods for the control, barren, forest and sandy-soil experiments of cases 1, 2, 3 and 5

among the smaller precipitation thresholds of 0.2–1.6 mm, with the opposite for the larger precipitation thresholds (i.e., 6.4–25.6 mm). Moreover, the *ETS* values are higher (better skill) for each experiment through the first four thresholds, while the *fBIAS* values (frequency bias) are the lowest during this period. The opposite occurs for the larger precipitation thresholds, as the *ETS* values are relatively low, with the highest *fBIAS* values for these thresholds (Fig. 7). Overall, while results suggest the model tends to overestimate precipitation (all *fBIAS* > 1), an improved skill and accuracy in all five cases for the lighter precipitation thresholds is evident. Regarding the three sensitivity experiments, the overall conclusion is consistent with case 4 whereby the barren experiment has the highest skill for precipitation thresholds of 0.2–3.2 mm, with *fBIAS* values closer to one. The forest and sandy-soil experiments have a similar skill (lower than the barren experiment), which is also close to that of the control experiment.

3.1.2 Surface Air Temperature, Humidity, and Wind Speed

In addition to the verification of model-simulated precipitation, near-surface atmospheric variables at the land–atmosphere interface reflect changes of land-surface conditions on the atmosphere. The observed 2-m air temperature (T_2, °C), the 2-m specific humidity (Q_2, g kg^{-1}), and the westerly and southerly velocity components at 10-m height (U and V, respectively, m s^{-1}) are available in the NCEP observational dataset, and are used to verify all four model simulations in terms of *RMSE* and *BIAS* values, which are calculated for all grid points in the nested domain for karst and non-karst grid points. For ease in counting the karst grid points, the observational data are interpolated to the model grid, where changes in the simulations are generally notable for the karst regions and marginal for the surrounding non-karst regions. Figure 8 shows, for example, the results for the karst regions from case 4 at 3-h intervals during the two-day simulation (0000 UTC 29-09-2008–0000 UTC 01-10-2008), with results from all five cases shown in Table 2. Note that the control results are indiscernible from the sandy-soil results in Fig. 8 for the case 4 variables analyzed.

For the surface atmospheric humidity (Fig. 8a), the WRF model normally (the control experiment) generates a positive bias throughout the day, and is further enhanced during the daytime by changes in land cover to forest. In contrast, the barren experiment largely corrects the daytime moist bias in the karst region, which, as shown in Table 2, is in agreement among all five cases.

For the 2-m air temperature, the control experiment displays a strong cold bias at night (Fig. 8b and Table 2). For the forest experiment, the bias worsens with increasing values
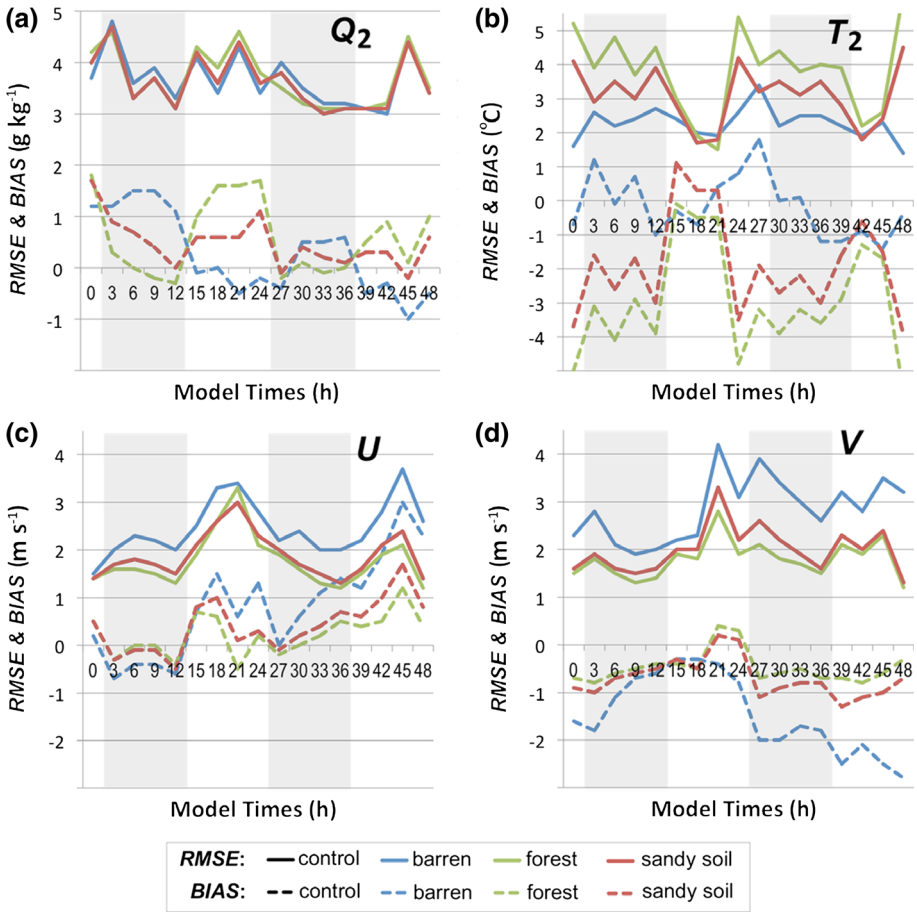
Fig. 8 Root-mean-square error and *BIAS* between model simulations and the NCEP observations over karst-only regions for: **a** surface air specific humidity Q_2 (g kg^{-1}), **b** surface air temperature T_2 (°C), **c** surface west-east velocity component U (m s^{-1}), and **d** surface south-north velocity component V (m s^{-1}). Results correspond to the control, barren, forest and sandy-soil experiments of case 4 from 0000 UTC 29 September 2008 to 0000 UTC 1 October 2008 at 3-h intervals. Grey shading indicates the night time. The control and sandy-soil experiments are indistinguishable

of *RMSE*, while the barren experiment shows a noticeable improvement by correcting the cold bias at night, and thus reducing the magnitude of the *RMSE* value. For the surface wind speeds (Fig. 8c, d, and Table 2), while the barren experiment produces larger errors than both the control and forest experiments, for case 4, the differences in wind speed are more likely the result of the large-scale synoptic variations. In addition, the overall results for the wind speeds shown in Table 2 may be dominated by the severe weather of case 5.

3.2 Model Sensitivity Analysis

Each model sensitivity to different land-cover and soil types in karst regions is compared with the control experiment. When different land and soil conditions are assumed for the karst landscape, complex model responses are expected, through which the performance of

Table 2 Average values of *RMSE* and *BIAS* of model-simulated surface air specific humidity (Q_2, g kg^{-1}), 2-m surface air temperature (T_2, °C), and 10-m wind speed (U, V, m s^{-1}) over karst areas from the control, barren, forest and sandy-soil experiments of all five cases, as calculated separately for day and night (for five cases, there is a total of 45 3-h day points and 40 3-h night points)

	Day				Night			
	Control	Barren	Forest	Sandy soil	Control	Barren	Forest	Sandy soil
Q_2								
RMSE	3.29	*2.63****	3.73	3.57	2.92	*2.86*	2.97	3.00
BIAS	1.79	*−0.11****	2.47**	2.26	1.19	*1.09*	*1.13*	1.44
T_2								
RMSE	3.11	*2.85*	3.34	3.22	3.55	*2.68****	4.02***	*3.32**
BIAS	−0.77	*0.14****	− 1.36*	− 1.26	−2.60	*−1.10****	− 3.17***	*−2.37*
U								
RMSE	2.37	3.30***	*2.18*	*2.30*	1.94	2.72***	*1.78***	*1.92*
BIAS	0.85	1.40**	*0.67*	*0.78*	0.25	0.31	0.27	0.26
V								
RMSE	2.61	3.92***	*2.40*	*2.57*	2.35	3.56***	*2.10**	2.35
BIAS	0.20	0.66	*0.12*	*0.17*	0.32	0.86	*0.24*	0.32

Values in bold-italicized font denote improved results with respect to the control run. One, two, and three stars denote the unequal variance *t* test (assuming independent data points; Moser et al. 1989; Ruxton 2006) with significance levels of 90, 95 and 99%, respectively, for significant differences between the control experiment and each of the three other experiments. Observational data used are the NCEP automated data processing global upper air and surface weather observations

each model experiment may be explained by examining the near-surface atmosphere (e.g., latent and sensible heat fluxes, surface air temperature, humidity and wind speed), convective development and precipitation (e.g., *CAPE*, *CIN*), as well as a cross-sectional analysis of the equivalent potential temperature and atmospheric instability.

3.2.1 Surface Air Temperature and Dew Point

The surface air temperature (T_2) and dew point temperature (T_{d2}) from each of the three experiments are compared with those of the control simulation within the nested domain during the rainy period for each case, as these times are well into the model simulation period. To further emphasize the influence of karst areas, these variables are analyzed over both karst and non-karst areas, in addition to the entire nested domain, with the motivation to separate the localized impacts from those extending downstream, since only modifications to the karst areas are performed. To better understand the T_2 and T_{d2} differences among the entire domain versus the karst and non-karst areas, the root-mean-square difference (*RMSD*) and *BIAS* values for T_2 and T_{d2} are calculated for each particular consideration and for each of the three experiments with respect to the control experiment. The calculation of *RMSD* and *BIAS* values for the entire nested domain uses all grid points, while only the karst and non-karst grid points are used for the calculation of karst and non-karst areal *RMSD* and *BIAS* values, respectively. These are illustrated in Fig. 9 for each of the three experiments for T_2 and T_{d2}, which are averaged over all 6-h time periods and all five cases. While the values of *RMSD* indicate the extent to which the modelling result of an experiment deviates from
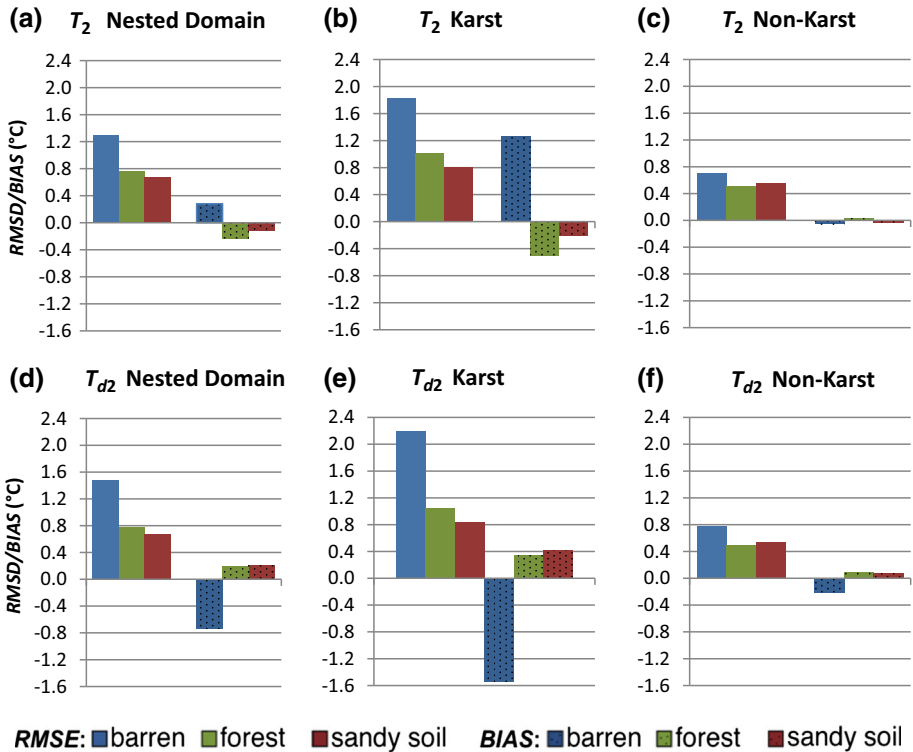
Fig. 9 Root-mean-square difference (°C) and *BIAS* (°C) between the barren, forest, sandy-soil and control experiments for the surface air temperature (T_2, **a–c**) and dew point temperature (T_{d2}, **d–f**) evaluated over the entire nested domain (**a, d**), karst areas (**b, e**), and non-karst areas (**c, f**). Results are averages over all 6-h time periods for all five cases

the control experiment, a positive (negative) *BIAS* value implies a warmer (cooler) or more (less) humid surface air than the control experiment.

With regard to T_2 for the entire nested domain (including both karst and non-karst regions), the *RMSD* value for the barren experiment increases by 1.3 °C compared with the control experiment (Fig. 9a), while the forest and sandy-soil experiments result in reduced values of 0.75 and 0.67 °C, respectively (Fig. 9a). When only karst areas are considered, all three experiments (barren, forest and sandy soil) respond similarly with larger magnitudes (compare Fig. 9a with b), with the barren experiment providing the greatest increase of 1.8 °C throughout (Fig. 9b). Both the forest and sandy-soil experiments show reduced temperatures of 1 and 0.8 °C over the karst areas, respectively, implying stronger cooling than over the entire nested domain (Fig. 9b). In non-karst areas where all experimental settings are the same as the control experiment (i.e. no changes made), the smallest impacts from each experiment are found (Fig. 9c), with the barren and sandy-soil experiments resulting in a small cooling and warming effect, respectively, which are opposite to the responses seen in karst areas (Fig. 9b). Thus, the overall impacts over the entire nested domain are dominated by the results shown for karst areas, implying a more localized impact from the karst regions.

The dew point temperature yields different results for the entire nested domain. The *BIAS* values in Fig. 9d indicate a drying effect for the barren experiment with a 0.7 °C

reduction in T_{d2}, while the forest and sandy-soil experiments both yield increases of 0.2 °C. The *RMSD* values are further changed when only karst areas are considered, with results suggesting additional lowering (i.e., drier) of T_{d2} for the barren land (-1.5 °C) with slightly moister responses for the forest (0.3 °C) and sandy-soil (0.4 °C) experiments compared with the control simulation. With non-karst areas having the same experimental settings as the control experiment, significantly smaller responses are detected than for karst areas. Over non-karst areas, the barren experiment gives a slight drying, while both the forest and sandy-soil experiments result in a minor moistening effect.

In summary, clear differences in sensitivity responses between the karst and non-karst regions are detected, with varying responses for both T_2 and T_{d2}, and differences for the barren experiment showing a noticeable T_2 increece and T_{d2} decrease across the karst areas (Figs. 9b, e). Interestingly, both the forest and sandy-soil experiments show a reduced T_2 across the karst areas (Fig. 9b), with an increased T_{d2}. The magnitude of T_2 across non-karst areas is much smaller with nearly negligible changes, as barren and sandy-soil experiments result in a slight cooling effect, while the forest has a minor warming effect (Fig. 9c). Similar results are found for T_{d2}, as non-karst areas with the barren experiment result in a drier atmosphere, while the forest and sandy-soil experiments both give a slightly moister atmosphere. Overall, T_2 and T_{d2} give clear changes linked to karst area simulations (Fig. 9a, d).

Figure 10 shows the spatial distributions of differences in T_2 and T_{d2} for the barren–control, forest–control, and sandy-soil–control experiments at 0000 UTC 30 September 2008, which is 1800 local standard time and 12 h into the rainy period of case 4 (Table 1). Here, T_2 has large positive differences of 3–8 °C for the barren experiment, and thus a warming of the karst areas (Figs. 1a, 10a). The vegetation in the control experiment consists of a large area of deciduous broadleaf within the nested domain (Fig. 1b), resulting in larger latent heat fluxes as discussed in detail in the following section. For the barren experiment, the sparse or total lack of vegetation cover results in more energy partitioned into the sensible heat flux, leading to the positive differences in T_2 (Fig. 10a).

The magnitudes of T_{d2} differences are unlike those of T_2, as larger negative differences of -2 to -7 °C occur along the karst areas (Figs. 1a, compare 10b with a). While T_2 differences are positive across karst areas, T_{d2} differences are large and negative, indicating drier conditions (Figs. 1a, 10a, b). It is worth noting that this time (0000 UTC 30 September 2008), is halfway through the rainy period (12 h into the 24-h period observed) (Table 1, Fig. 10b). Once the precipitation from the mesoscale convective system affects these areas, moderate rain continues to fall across the nested domain, resulting in larger negative differences due to the cooler, drier air behind the leading edge of precipitation (see Figs. 2b, 10b).

The forest experiment produces larger negative differences in T_2 of -1 to -4 °C across the karst areas (Figs. 1a, 10c) as the forest cover provokes cooler conditions (Figs. 1a, 10c). Although T_2 in the forest simulation is slightly lower than that of the control experiment, larger positive differences in T_{d2} of 1–4 °C are found (Figs. 1a, 10d). Throughout the nested domain, much wetter conditions are found for the karst areas covered by a forest canopy (Figs. 1a, 10d), which increases evapotranspiration and thus leads to increased atmospheric moisture (Fig. 10d).

Interestingly, T_2 and T_{d2} from the sandy-soil experiment show negligible differences compared with the control simulation within the nested domain (Figs. 1a, 10e, f). Sandy soil is the most porous of all soil types, becoming drier more quickly than any other type (Oke 1987). Since the land-cover type is kept the same as the control simulation, the negligible changes to T_2 and T_{d2} suggest that the land-cover type dominates the land–atmosphere feedback, which may suppress impacts from different soil types.
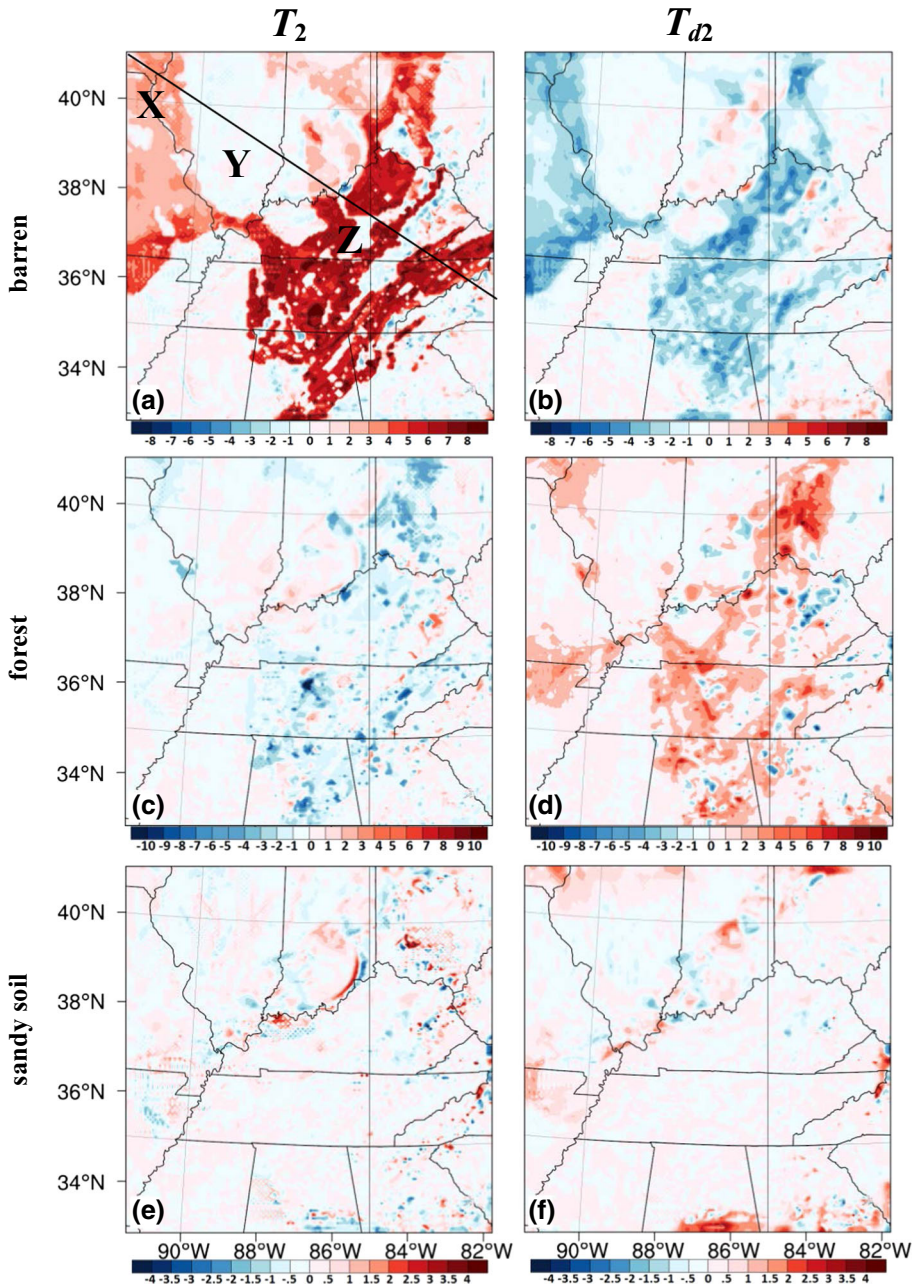
Fig. 10 Differences between barren-control (**a**, **b**), forest-control (**c**, **d**), and sandy-soil–control (**e**, **f**) experiments for case 4, over the nested domain at 0000 UTC 30 September 2008: **a**, **c**, **e** surface air temperature (T_2, °C); **b**, **d**, **f** dew point temperature (T_{d2} °C). The line XYZ in **a** marks the location for cross-sectional analysis with non-karst (Y) and karst (X, Z) areas

3.2.2 Latent and Sensible Heat Fluxes

As land–atmosphere interactions involve exchanges of mass and heat, and, therefore, latent (Q_E) and sensible (Q_H) heat fluxes as illustrated in Fig. 11, where the *RMSD* and *BIAS* values between each of the three experiments and the control experiment for Q_E and Q_H, are averaged over all five cases. For the entire nested domain, the *RMSD* and *BIAS* of Q_E for the barren experiment indicates a large decrease of 32 W m^{-2} when compared with the control experiment (Fig. 11a), while the forest and sandy-soil experiments result in small increases of 9 W m^{-2} and 2 W m^{-2}, respectively (Fig. 11a). Responses are very distinct when only the karst areas are considered, as the barren experiment shows an even larger decrease than the entire nested domain of 55 W m^{-2} (compare Fig. 11b with a). It should be noted that, compared with the entire nested domain, the forest and sandy-soil experiments give larger Q_E increases of 24 W m^{-2} and 4 W m^{-2} in the karst areas, respectively (compare Fig. 11b with a). As non-karst areas show the smallest, but opposite, effect from each experiment (Fig. 11c), the overall impacts over the nested domain are dominated by the results related to the karst area, again implying a localized impact from karst regions.

In comparison with the T_{d2} responses shown in Fig. 10b, d, f, it is clear that the moisture transferred from the land surface to the atmosphere is associated with Q_E, which results in a change in atmospheric humidity. In comparison with the control experiment, the Q_E partitioning for the barren experiment decreases, causing drier near-surface atmospheric
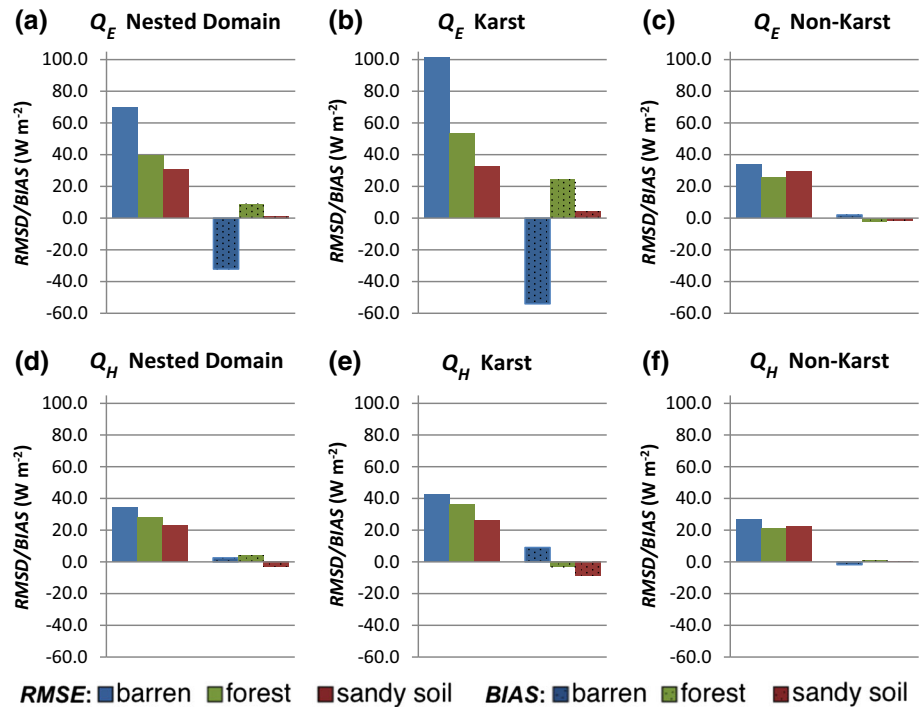

Fig. 11 Root-mean-square difference (W m^{-2}) and *BIAS* (W m^{-2}) between the barren, forest and sandy-soil experiments and the control experiment for the latent heat flux (**a–c**) and sensible heat flux (**d–f**) evaluated over the entire nested domain (**a, d**), karst areas (**b, e**), and non-karst areas (**c, f**). Results are averages over all 6-h time periods of all five cases

conditions with reduced T_{d2} over the karst areas. The forest and sandy-soil experiments produce a higher upwards Q_E, resulting in moister near-surface atmospheric air over the karst areas. In addition, the impacts of land-type changes on Q_E and near-surface humidity are primarily local as shown by the minimal responses over the non-karst areas.

Furthermore, the values of Q_H for the entire nested domain are less distinct (compare Fig. 11d with a). However, the *RMSD* and *BIAS* values for both the barren and forest experiments indicate a slight increase in Q_H of 2 and 4 W m^{-2}, respectively, across the entire nested domain (Fig. 11d). While both the barren and forest experiments provide slight increases for the entire nested domain, the sandy-soil experiment produces a decrease of 3 W m^{-2} (compare Fig. 11d with a). When karst areas are considered, the values of Q_H increase by 9 W m^{-2} for the barren experiment, with larger decreases of 3 and 9 W m^{-2} for forest and sandy-soil experiments, respectively. For the non-karst areas, opposite but negligible changes are found when compared with the karst areas and the entire nested domain (compare Fig. 11f with d, e).

In comparison with the T_2 responses in Fig. 10a, c, e, we find that Q_H is a significant factor for the surface air temperature, resulting in changes dependent on the particular experiment. When compared with the control experiment, the barren experiment gives an increased sensible heat flux, causing warmer surface conditions with an increased T_2 over karst areas. However, both the forest and sandy-soil experiments produce a smaller Q_H, leading to a cooler surface temperature over the karst areas. Similar to Q_E and the surface humidity, impacts on Q_H and air temperature are also local, with marginal responses over non-karst areas.

As an example, Fig. 12 presents the spatial distributions in both latent and sensible heat fluxes for the barren-control, forest-control, and sandy-soil-control experiments for case 4 at 1800 UTC 29 September 2008, which is noon local standard time and 6 h into the rainy period. Note that the timestamps are different than that of T_2 as Q_H typically shows the smallest changes around sunset or sunrise, but larger during the middle of day or at night. Moreover, Fan (2009) found that the heat flux converges and produces the temperature change.

The barren experiment for case 4 generates negative Q_E differences of -160 to -200 W m^{-2} from the control experiment across the karst areas in the entire nested domain (Figs. 1a, 12a). Areas including central Illinois and Indiana provide positive differences of 40–100 W m^{-2} outside of the karst areas where the land cover consists of mostly cropland and deciduous broadleaf forests (Figs. 1a, b, 12a). These noisy, but localized, distributions, with some horizontal patterns, indicate that the differences are mostly likely caused by the weather system (i.e., changes within the atmosphere), which moved to the south-east from the north-west of the domain. However, the barren land (for karst areas) results in positive Q_H differences in the spatial distribution across the nested domain (Figs. 1a, 12b). Note that this time is 6 h into the rainy period and T_2 is still high (Fig. 10a). Thus, it is possible that several karst areas show a negative difference in Q_H. More detailed examination shows that Q_H is more intermittent over the karst areas, with positive differences occurring along the karst and non-karst boundaries (Figs. 1a, 12b). The negative and positive differences along these boundaries may be attributed to the sharp transition from barren land to vegetation (Fig. 12b).

Unlike the barren experiment, the forest experiment provides large positive Q_E differences of 100–200 W m^{-2} over the karst areas, which is expected (Fig. 12c). In contrast, Q_H over the karst areas gives positive differences of 40–120 W m^{-2}, with a slight increase over central and west Kentucky when compared with the barren experiment (compare Fig. 12d with b). Figure 12d also shows even stronger positive differences of 40–160 W m^{-2} across central Tennessee. Overall, modelling results show that forests have a cooling effect through the increased
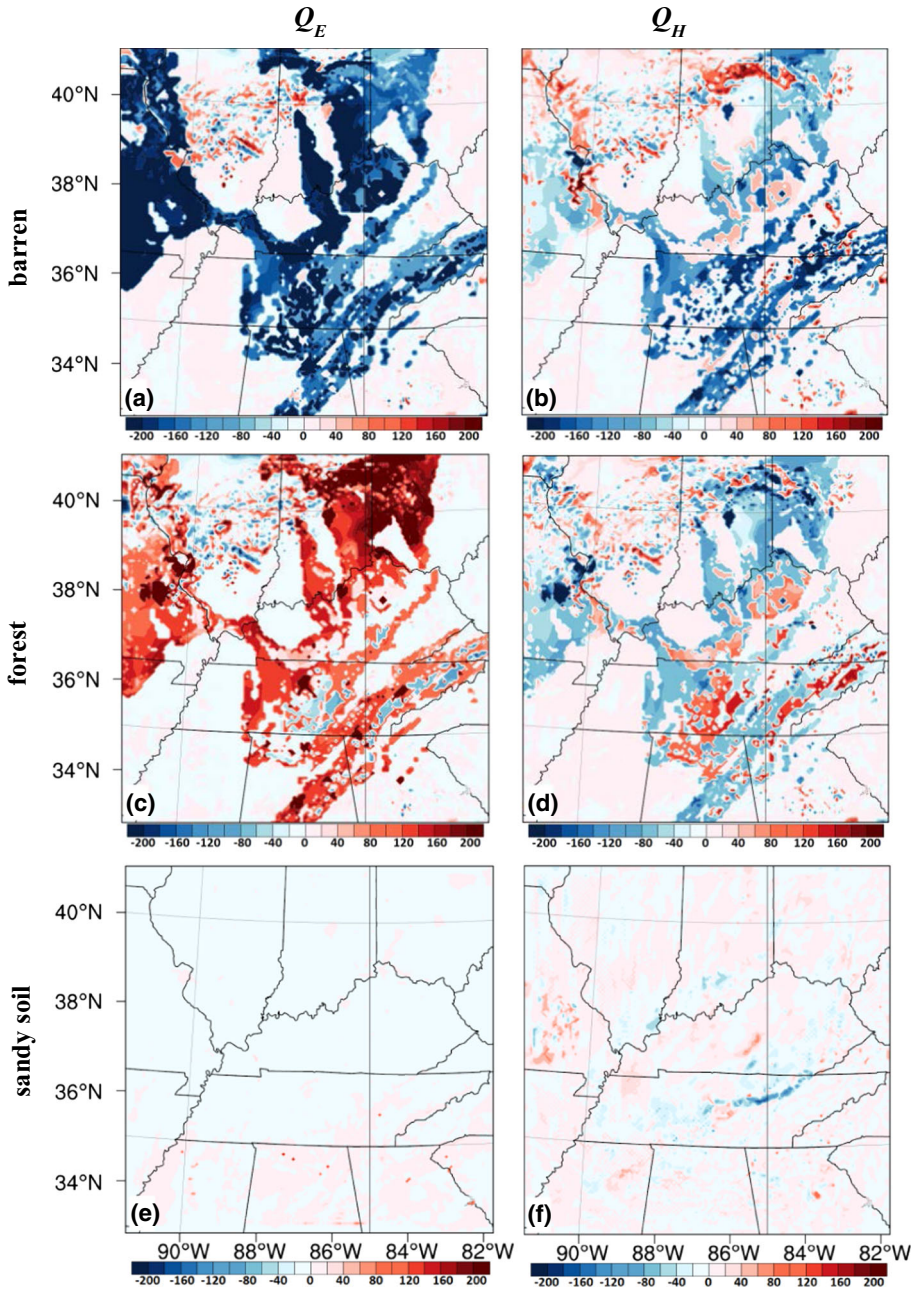
Fig. 12 Spatial distribution for the barren-control (**a**, **b**), forest-control (**c**, **d**) and sandy-soil-control (**e**, **f**) experiments for case 4 over the nested domain at 1800 UTC 29 September 2008: **a**, **c**, **e** latent heat flux (W m^{-2}); **b**, **d**, **f** sensible heat flux (W m^{-2})

Q_E. The sandy-soil experiment provides overall minimal differences in Q_E, Q_H, T_2 and T_{d2} across the nested domain (Figs. 1a, 12e, f).

3.2.3 Convective Available Potential Energy and Convective Inhibition

The values of *CAPE* and *CIN* help assess the evolution and development of precipitation, with differences in maximum *CAPE* and *CIN* of an atmospheric column between the barren and control experiment for case 4 shown in Fig. 13. As case 4 features a mesoscale convective system, which propagates from the north-west of the nested domain to the south-east during the experiment (see Fig. 2d), strong negative *CAPE* differences of -400 to -800 J kg^{-1} across sections of Missouri and Illinois and intermittent positive differences of 400–800 J kg^{-1} in central Indiana, south Illinois, and west Kentucky are detected (Fig. 13a, b). The strongest positive *CAPE* differences of 600–800 J kg^{-1} occur along west Kentucky and into west Tennessee during the middle of the rainy period (Table 1, Fig. 13c). The larger positive and negative values of *CAPE* move to the south-east into central Tennessee and north Alabama through the rainy period (Table 1, Fig. 13d, e). The *CAPE* estimates are reasonable and represent the leading edge of the mesoscale convective system while propagating to the south-east (Fig. 13d, e). Figure 13b shows the onset of larger positive *CAPE* differences from central Indiana and southwards along the Ohio River, indicating the leading line of the convective storm maximizes all the atmospheric energy for storm initiation, and, consequently, the south-east progression of enhanced values of *CAPE* and precipitation (Figs.2d, 13a–e).

The *CIN* values are less distinct across the nested domain for this event. Throughout much of the rainy period, intermittent *CIN* values are present over west Kentucky and Tennessee (see Fig. 13f, g and Table 1), and continue propagating across Tennessee and eventually into north Alabama towards the end of the rainy period (see Table 1, Fig. 13h–j). Along areas of large negative differences in *CAPE*, some positive *CIN* differences also occur, which indicates suppression of the convection (Fig. 13a–c, f–h), while the opposite is found for larger positive *CAPE* values, with negative *CIN* values indicating potentially enhanced convection (see Fig. 13b, c, g, h). A similar observation and assessment applies to the *CIN* values has intermittent positive and negative differences occur along the leading edge of the precipitation system (Fig. 13g–i). As both *CAPE* and *CIN* values coincide well with one another, the most
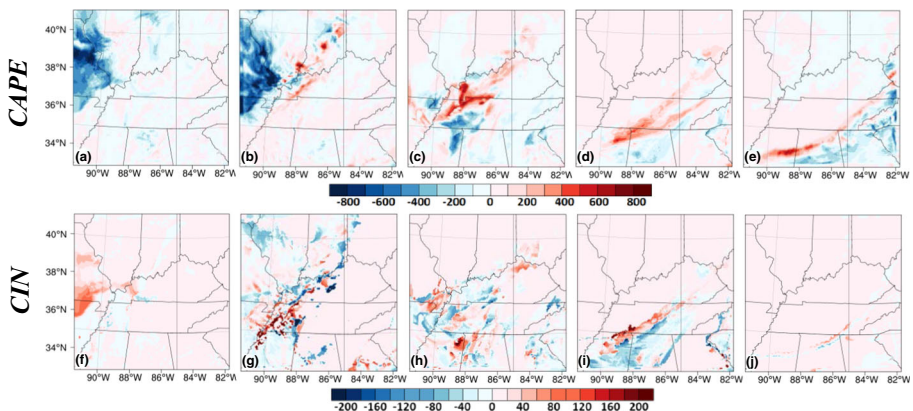

Fig. 13 Differences between the barren and control simulations for case 4 over the nested domain at 6-h intervals from 1800 UTC 29 September 2008 to 1800 UTC 30 September 2008: **a–e** *CAPE* (J kg^{-1}); **f–j** *CIN* (J kg^{-1})

noticeable differences occur along the frontal line of precipitation (compare Fig. 13a–e with f–i). Overall, it appears that the barren experiment for both the column maximum *CAPE* and *CIN* values has no real influence across the near-surface atmosphere as they follow the leading edge of the precipitation from the mesoscale convective system closely throughout the rainy period (see Figs. 2d, 13). This implies that both convective parameters are largely controlled by larger, synoptic conditions. The analysis along a vertical cross-section in the next section further reveals the responses of the magnitude of *CAPE* to the land-cover changes in both the barren and forest experiments.

3.2.4 Vertical Cross-Section Analysis

The investigation of vertical cross-sections aids in understanding possible near-surface land–atmosphere feedbacks. The location of the cross-section is marked in Fig. 10a, with X, Y and Z representing karst, non-karst, and karst sections, respectively, along the propagation of the system from the north to the south. Therefore, the effects across both karst and non-karst areas for the barren and forest experiments may be examined.

Figure 14 shows vertical cross-sections from the comparison of barren and forest experiments with the control experiment for the analysis of the near-surface conditions for temperature (T_{air}, °C), moisture (water vapour mixing ratio Q_V, g kg^{-1}), equivalent potential temperature (θ_e, °C), vertical circulation, and *CAPE* values at 0600 UTC 29 September 2008, which is 9 h after model initialization and 6 h before the rainy period, so that the changes in land-cover types have taken effect during the first 9 h of integration, and yet have not been notably affected by the more intense precipitation.

(a) Air Temperature and Specific Humidity

For the cross-section of air temperature T_{air} shown in Fig. 14a, the first kilometre of the atmosphere at point X shows mostly positive differences between the barren and control experiments. Relatively small differences are shown across point Y, which features mainly non-karst areas, and hence the land cover is the same as for the control run (Figs. 10a, 14a). However, relatively large negative differences of -0.2 to -0.4 °C are present close to the boundary of X and Y, which is indicative of the leading edge of the precipitation system resulting in rain-cooled air. At location Z, results correspond well with the previous analysis for the barren experiment as large positive differences of $0.6-1$ °C are noted over the karst areas (Figs. 10a, 14a), with an intense warming effect for the barren experiment over the karst areas resulting in warmer surface conditions (Fig. 14a). The forest cross-sectional analysis features the exact opposite results compared with the barren experiment, with a large cooling of -0.2 to -1 °C near the surface over karst areas (Figs. 10a, 14b; points X and Z), which are represented well across both locations over karst areas, while small differences are once again seen over the non-karst areas (point Y; Figs. 10a, 14b).

Differences in Q_v through the barren-control and forest-control comparisons (Fig. 14c, d) generally match the results from the T_{d2} and Q_E spatial analyses (Figs. 10b, d, 12a, c). Small differences are noted across non-karst areas (point Y), but negative differences ranging from -0.4 to -0.8 g kg^{-1} are also shown for the barren experiment over karst areas (Figs. 10a, 14c; points X and Z). This vertical cross-section supports the results for the barren experiment initiating drier near-surface conditions (Figs. 9e, 10b, 14c), which is not as clear at point X as at Z, since the precipitation system has moved into point X by this time. The forest experiment shows larger positive differences of 0.4 to 1.2 g kg^{-1}, indicating moister surface conditions (Figs. 9e, 10d, 14d). As noted previously, larger magnitudes of differences
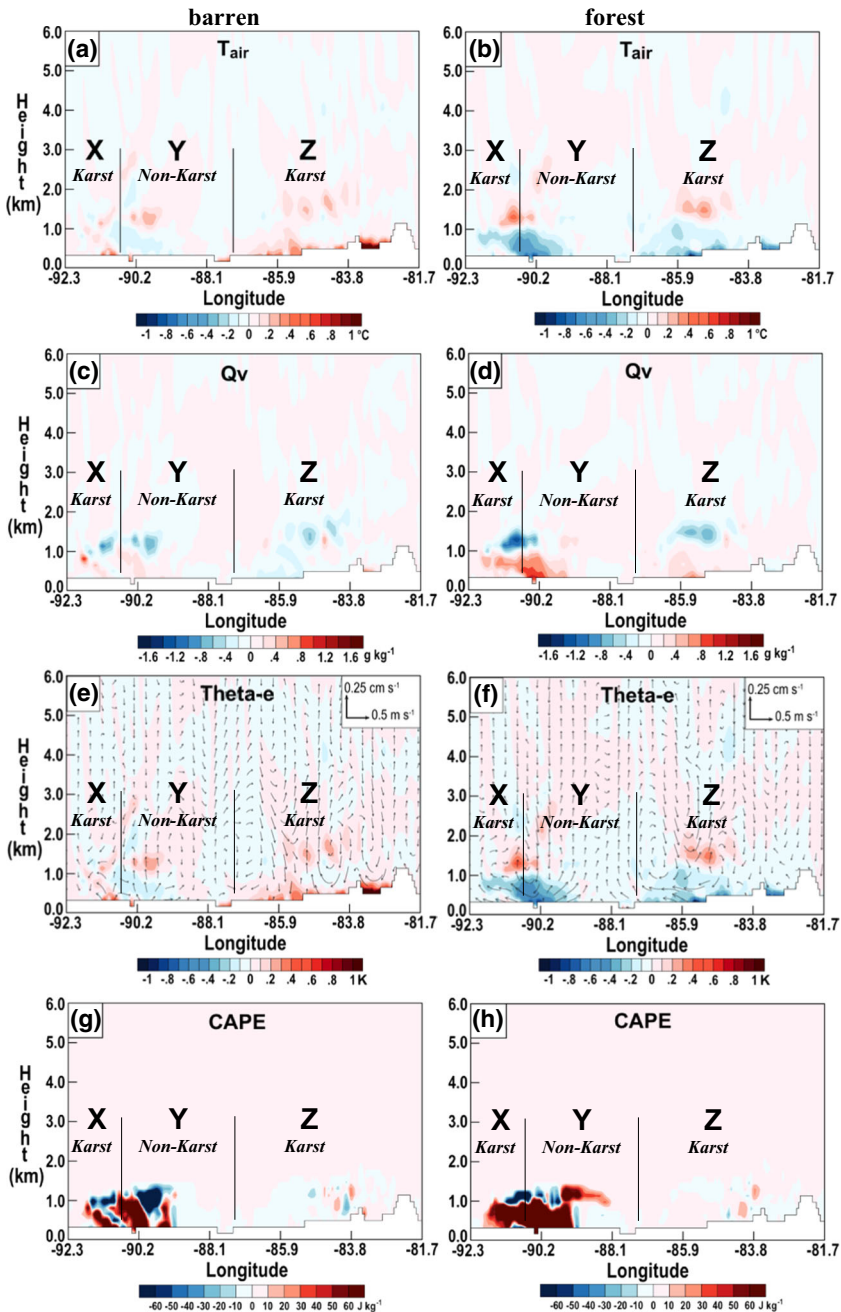
Fig. 14 Differences between the barren and control experiments (**a**, **c**, **e**), and the forest and control experiments (**b**, **d**, **f**) for case 4 along the vertical cross-section XYZ marked in Fig. 10a at 0600 UTC 29 September 2008: **a**, **b** air temperature (T_{air}, °C); **c**, **d** water vapour mixing ratio (Q_v, g kg^{-1}); **e**, **f** equivalent potential temperature (θ_e, °C) and vertical circulation (reference vectors shown at upper-right corners); **g**, **h** *CAPE* (J kg^{-1}) at each grid point. The line XYZ in Fig. 10a marks the location of the cross-sectional analysis where non-karst (Y) and karst (X, Z) areas begin and end

are found mostly across the karst areas (points X and Z) and within the surface layer with little to no differences aloft (Figs. 10a, 14a–d).

(b) Equivalent Potential Temperature

Equivalent potential temperature (θ_e) or moist static energy differences for both the barren and forest experiments yield further stability information (e.g., Pielke 2001) (Fig. 14e, f), where, as mentioned above, the barren experiment provides positive differences in near-surface temperature across karst regions (points X and Z). Likewise, the barren experiment results in large positive differences in θ_e of 0.4–1 °C across the surface over the karst areas (Fig. 14e; points X and Z). Although there is a drying effect from the barren experiment over the karst areas, which may reduce θ_e, the warming effect obviously plays a dominant role in the changes of θ_e. The changes of θ_e are just the opposite for the forest experiment, where the above analysis shows negative differences in temperature (a cooling effect) across the surface, but larger positive differences for Q_v (points X and Z; compare Fig. 14b, d with a, c). However, when considering θ_e, the cross-sectional analysis reveals strong negative differences of -0.6 to -1 °C across the karst areas, especially near the surface, where the cooling effect is the strongest (point Z; compare Fig. 14b with f). Vertical profiles of θ_e relate to the potential instability of the atmosphere (e.g., Petty 2008). The θ_e values within the boundary layer imply that a barren surface increases the potential instability (from the warming and increased near-surface θ_e over the karst areas), while forest cover decreases the potential instability near the surface.

(c) Vertical Circulation

The vertical circulation within the cross-sectional plane helps determine if any significant low-level circulations are generated from the experiments (Fig. 14e, f). Both the barren and forest experiments generate differences as large as 0.5 m s^{-1} in the horizontal and 2.5 mm s^{-1} in the vertical velocity components, with largest changes found in the karst area (point Z) and in the vicinity of the precipitation system (points X and Y). For the forest experiment, near-surface cooling and the decreased potential instability (as seen from θ_e) leads to an overall enhanced downdraft over both point Z and the precipitation system area, resulting in near-surface flow divergence at points X and Z, so that the rising motion dominates at point Y (the non-karst area). The barren experiment shows less pronounced flow patterns (Fig. 14e) than the forest experiment, while weak circulation patterns opposite to that of the forest experiment are still discernable. The vertical circulation patterns suggest a correspondence to the precipitation patterns in the barren and forest experiments. At 0600 UTC 29 September 2008, the precipitation system at point X extends into part of the non-karst areas of point Y, where all model-simulated precipitation is similar (Figs. 3, 14). Recall that both the control and forest experiments overestimate the total precipitation at locations with heavy rainfall, which are mostly located near the non-karst areas of point Y. Consistent with Quintanar et al. (2008) and Suarez et al. (2014), the enhanced updraft for the forest experiment at point Y directly leads to enhanced precipitation, while the barren experiment improves the simulation of precipitation by correcting the overestimation seen in the control and forest experiments (see the discussion in Sect. 3.1).

(d) Convective Available Potential Energy and Associated Instability

As discussed above in Sect. 3.2, the differences in maximum *CAPE* values of atmospheric columns are mainly the result of the large synoptic-scale progression of the precipitation system, with no obvious impacts from the localized land-surface conditions. However, the case is different when analyzing *CAPE* values along cross-sections and within the planetary

boundary layer. Figure 14g, h show *CAPE* (of an air parcel at each grid point) differences within the lower layers of the atmosphere from the barren-control and forest-control comparisons, respectively. The leading edge of the precipitation line can easily be distinguished as very large differences occur there (Figs. 10a, 14g, h), with mostly very small differences occurring across the non-karst areas in the barren experiment ahead of this line (point Y, Figs. 10a, 14g). Vertical profiles give more interesting results over karst areas (points X and Z) as more frequent negative *CAPE* values are found in the barren experiment near the surface. The forest experiment provides similar impacts as the barren experiment, but with more positive differences in *CAPE* values over the karst areas (Fig. 14h).

As the cross-sections of *CAPE* and Q_v values (compare Fig. 14g, h, with c, d) show patterns that align well, we suggest that the humidity plays a dominant role in determining the magnitude of *CAPE*, which agrees with earlier studies (e.g., Pielke 2001; Collow et al. 2014). With the drying effect of karst areas in the barren experiment, the values of *CAPE* decrease, and, consequently, the instability is suppressed, which further leads to the reduction in precipitation. Similarly, the wetting effect of the forest experiment leads to increased *CAPE* values, local instability and, consequently, enhanced precipitation.

4 Discussion and Conclusions

The impacts of karst landscapes on five precipitation events and the related atmospheric variables are assessed by comparing modelling results from different land types for simulating rainfall over karst and non-karst areas. Since existing models do not distinguish between karst and non-karst areas, the experiments help determine which existing land types in the model, along with their physical parameters, result in improved rainfall simulations in karst regions. Note that the changes introduced in the modelling experiments are limited to karst regions only. Subsequently, by using relatively similar barren land cover and sandy-soil conditions from the existing model to mimic certain karst characteristics, along with a contrasting forest land cover, the WRF model reveals a potential influence from the karst terrain under various weather conditions. Even though small perturbations at the initiation times of the modelling runs may cause small changes to the simulations, both the barren and forest land covers provide feedback through the exchange of heat and moisture at the surface, and show the potential for modified convective development based on several convective parameters, including T_2, T_{d2}, T_{air}, Q_v, θ_e, and *CAPE*.

Overall, as shown in Fig. 15, the impacts of land cover and soil types over karst regions on the boundary layer are summarized as a simplified conceptual model (Winchester et al. 2017). The barren experiment results in the largest changes in both T_2 and T_{d2}, where a strong warming effect occurs with an intense drying effect across the karst region. These results contradict those of the forest experiment, as lower T_2 with much wetter near-surface conditions are found over karst areas. The drying effect for the barren experiment is more prominent during the day, while the warming effect is significant during both day and night. Analysis for both latent and sensible heat fluxes further supports these findings, as a large decrease in near-surface moisture is apparent for the barren experiment, while a slight increase is seen in the forest and sandy-soil experiments. The warming and cooling effects in the barren and forest experiments are linked to increased and decreased sensible heat fluxes, respectively. The warming effect for the barren experiment over the karst areas ultimately leads to increased potential instability, while the forest experiment gives the opposite result, with a decrease in potential instability due to surface cooling. These thermally-induced instabilities related
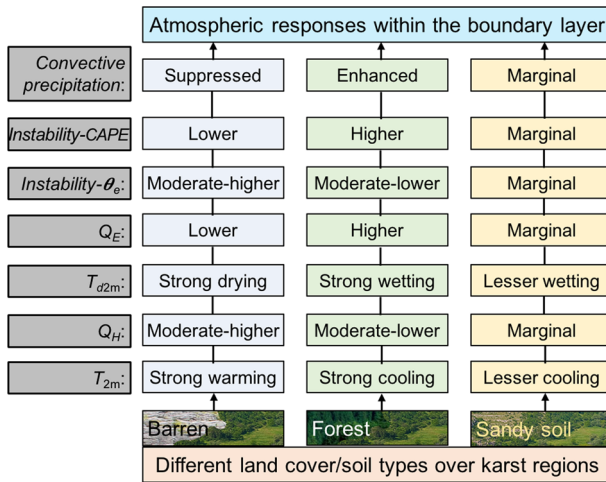
Atmospheric responses within the boundary layer

	Barren	Forest	Sandy soil
Convective precipitation:	Suppressed	Enhanced	Marginal
Instability-CAPE	Lower	Higher	Marginal
Instability-θ_e:	Moderate-higher	Moderate-lower	Marginal
Q_E:	Lower	Higher	Marginal
T_{d2m}:	Strong drying	Strong wetting	Lesser wetting
Q_H:	Moderate-higher	Moderate-lower	Marginal
T_{2m}:	Strong warming	Strong cooling	Lesser cooling
	Barren	Forest	Sandy soil

Different land cover/soil types over karst regions

Fig. 15 A simplified conceptual model of atmospheric responses within the boundary layer to different land cover/soil types over karst regions (note: the changes are all relative to the control experiment)

to vertical circulation patterns enhance (e.g., in the forest experiment) or suppress (e.g., in the barren experiment) large-scale convection traversing non-karst and karst boundaries. In contrast, the values of *CAPE* show a close relationship with atmospheric humidity, while being related to the local instability. Thus, the drying effect for the barren experiment leads to a decrease in the values of *CAPE*, as well as instability, and contribute to the correction of the overestimation of precipitation in the control experiment. Again, the forest experiment produces the opposite effect.

While the carbonate rocks composing karst landscapes cover some 18% of the land area of the USA (Weary and Doctor 2014) within a range of climates, and have been shown to influence land–atmosphere interactions, a full set of karst-related inputs for a land-surface model for atmospheric simulations have not yet been developed. Our research builds on recent studies using existing model input parameters to explore relationships between karst areas and land-cover types for the possible improvement in model representation and the simulation of precipitation. The use of the barren and sandy-soil land covers in the model represent one aspect of typical karst hydrologic conditions, wherein thin soils and highly permeable bedrock beneath often result in rapid drainage through the soil, and provide a basis for developing an optimal land-cover parametrization for karst terrain.

We recommend: (1) future work to develop methods for realistically representing karst landscapes; (2) field campaigns to collect data to further understand and quantify karst hydrology and model verification; (3) the inclusion of karst soil hydrological processes in models (see introduction); (4) the introduction of appropriate model tables representing soil hydrological properties; (5) appropriate descriptions of vertical water transport through the soils and bedrock of karst landscapes, including the fluxes of water vapour (Gonzalez et al. 2012); (6) modifications in land-cover and soil types, and their testing through experiments under various weather conditions; and (7) close collaboration between karst hydrologists and atmospheric scientists during model development.

Since the conclusions from our five cases could still be somewhat biased, seasonal or even longer periods of simulation are recommended. Although it is quite common to have a short model spin-up time, we recognize the need for much longer model (especially the

land-surface model) spin-up times of weeks to years in duration (Cosgrove et al. 2003; Rodell et al. 2005; Chen et al. 2007; Case et al. 2008; Santanello et al. 2013; Angevine et al. 2014; Best and Grimmond 2014; Lawston et al. 2015), which is particularly helpful in improving model hydrology and flux estimations, and is typically conducted by running the land-surface model offline.

References

Angevine WM, Bazile E, Legain D, Pino D (2014) Land surface spinup for episodic modeling. Atmos Chem Phys 14(15):8165–8172

Best M, Grimmond CSB (2014) Importance of initial state and atmospheric conditions for urban land surface models' performance. Urban Clim 10:387–406. doi:10.1016/j.uclim.2013.10.006

Bonacci O, Pipan T, Culver DC (2009) A framework for karst ecohydrology. Environ Geol 56:891–900

Bonan GB (2008) Forests and climate change: forcings, feedbacks, and the climate benefits of forests. Science 320(5882):1444–1449

Case JL, Crosson WL, Kumar SV, Lapenta WM, Peters-Lidard CD (2008) Impacts of high-resolution land surface initialization on regional sensible weather forecasts from the WRF model. J Hydrometeorol 9(6):1249–1266

Chen F, Dudhia J (2001) Coupling an advanced land surface–hydrology model with the Penn State–NCAR MM5 modeling system. Part I: model implementation and sensitivity. Mon Weather Rev 129:569–585

Chen F, Manning KW, LeMone MA, Trier SB, Alfieri JG, Roberts R, Tewari M, Niyogi D, Horst TW, Oncley SP, Basara JB (2007) Description and evaluation of the characteristics of the NCAR high-resolution land data assimilation system. J Appl Meteorol Climatol 46(6):694–713

Chou MD, Suarez MJ, Ho CH, Yan MMH, Lee KT (1998) Parameterizations for cloud overlapping and shortwave single-scattering properties for use in general circulation and cloud ensemble models. J Clim 11:202–214

Clark CA, Arritt RW (1995) Numerical simulations of the effect of soil moisture and vegetation cover on the development of deep convection. J Appl Meteorol 34:2029–2045

Collow TW, Robock A, Wu W (2014) Influences of soil moisture and vegetation on convective precipitation forecasts over the United States Great Plains. J Geophys Res Atmos 119:9338–9358. doi:10.1029/2014JD021454

Cosgrove BA, Lohmann D, Mitchell KE, Houser PR, Wood EF, Schaake JC, Robock A, Marshall C, Sheffield J, Duan Q, Luo L (2003) Real-time and retrospective forcing in the North American Land Data Assimilation System (NLDAS) project. J Geophys Res Atmos 108(D22):GCP3-1

Crowther J (1987) Ecological observations in tropical karst terrain, West Malaysia. III. Dynamics of the vegetation-soil-bedrock system. J Biogeogr 14:157–164

Dai Y, Dai Y, Zeng X, Dickinson RE, Baker I, Bonan GB, Bosilovich MG, Denning AS, Dirmeyer PA, Houser PR, Niu G, Oleson KW (2003) The common land model. Bull Am Meteorol Soc 84:1013–1023

Davies WE, Simpson JH, Ohlmacher GC, Kirk WE, Newton EG (1984) Digital engineering aspects of Karst Map. U.S. Geological Survey, National Atlas of the United States of America, GIS version by Tobin BD and Weary DJ. http://pubs.usgs.gov/of/2004/1352/

Durkee JD, Campbell L, Berry K, Jordan D, Goodrich G, Mahmood R, Foster S (2012) A synoptic perspective of the record 1–2 May 2010 mid-South heavy precipitation event. Bull Am Meteorol Soc 93(5):611–620

Fan X (2009) Impacts of soil heating condition on precipitation simulations in the Weather Research and Forecasting model. Mon Weather Rev 137:2263–2285

Ford D, Williams PD (2007) Karst hydrogeology and geomorphology. Wiley, New York, 576 pp

Fry J, Xian G, Jin S, Dewitz J, Homer C, Yang L, Barnes C, Herold N, Wickham J (2011) Completion of the 2006 national land cover database for the conterminous United States. PE& RS 77(9):858–864. http://www.mrlc.gov/nlcd2006.php

Gaines M (2012) Application of the weather research and forecasting (WRF) model to simulate a squall line: implications of choosing parameterization scheme combinations and model initialization data sets. Masters theses and specialist projects, paper 1181. http://digitalcommons.wku.edu/theses/1181

Gao J, Xue Y, Wu S (2013) Potential impacts on regional climate due to land degradation in the Guizhou Karst Plateau of China. Environ Res Lett 8(4):044037

Gonzalez GR, Verhoef A, Vidale PL, Braud I (2012) Incorporation of water vapor transfer in the JULES land surface model: implications for key soil variables and land surface fluxes. Water Resour Res 48:W05538. doi:10.1029/2011WR011811

Groves C (2007) Hydrological methods. In: Goldscheider N, Drew D (eds) Methods in karst hydrology. Taylor & Francis, London, pp 45–64

Groves C, Meiman J (2005) Weathering, geomorphic work, and karst landscape evolution in the Cave City groundwater basin, Mammoth Cave, Kentucky. Geomorphology 67:115–126

Groves C, Bolster C, Meiman J (2005) Spatial and temporal variations in epikarst storage and flow in south central Kentucky's Pennyroyal Plateau sinkhole plain. US Geol Surv Sci Investig Rep 2005–5160:64–73

Hartmann A, Barbera JA, Lange J, Andreo B, Weiler M (2013) Progress in the hydrologic simulation of time variant recharge areas of karst systems—exemplified at a karst spring in Southern Spain. Adv Water Resour 54:149–160

Heilman JL, McInnes KJ, Kjelgaard JF, Owens MK, Schwinning S (2009) Energy balance and water use in a subtropical karst woodland on the Edwards Plateau, Texas. J Hydrol 373:426–435

Hess JW, White WB (1989) Chemical hydrology. In: White WB, White EL (eds) Karst hydrology: concepts from the Mammoth Cave area. Van Nostrand Reinhold, New York, pp 145–174

Jackson RB, Moore LA, Hoffmann W, Pockman WT, Linder CR (1999) Ecosystem rooting depth determined with caves and DNA. Proc Natl Acad Sci 96(20):11387–92

Ji Y, Zhou G, Wang S, Wang L (2015) Increase in flood and drought disasters during 1500–2000 in Southwest China. Nat Hazards 77(3):1853–1861

Jiang Z, Yuan D (1999) CO_2 source-sink in karst processes in karst areas of China. Episodes 22(1):33–35

Kain J, Fritsch M (1993) Convective parameterization for mesoscale models: the Kain–Fritsch scheme. In: The representation of cumulus convection in numerical models. Meteorological monographs. American Meteor Society, vol 24, no 46, pp 165–170

Lawston PM, Santanello JA Jr, Zaitchik BF, Rodell M (2015) Impact of irrigation methods on land surface model spinup and initialization of WRF forecasts. J Hydrometeorol 16(3):1135–1154

Leeper R, Mahmood R, Quintanar AI (2011) Influence of karst landscape on planetary boundary layer atmosphere: a Weather Research and Forecasting (WRF) model-based comparison. J Hydrometeorol 12:1512–1529

Li E, Jiang Z, Cao J, Jiang G, Deng Y (2003) The comparison of properties of karst soil and karst erosion ratio under different successional stages of karst vegetation in Nongla, Guangxi. Acta Ecol Sin 24(6):1131–1139

Lin Y (2011) GCIP/EOP surface: precipitation NCEP/EMC 4KM gridded data (GRIB) stage IV data. Version 1.0. UCAR/NCAR—Earth Observing Laboratory. http://data.eol.ucar.edu/dataset/21.093. Accessed 04 March 2017

Lin YL, Farley RD, Orville HD (1983) Bulk parameterization of the snow field in a cloud model. J Clim Appl Meteorol 22:1065–1092

McPherson RA (2007) A review of vegetation-atmosphere interactions and their influences on mesoscale phenomena. Prog Phys Geogr 31:261–285

Meng H, Wang L (2010) Advance in karst hydrological model. Prog Geogr 11:006

Mesinger F et al (2006) North American regional reanalysis. Bull Am Meteorol Soc 87:343–360. doi:10.1175/BAMS-87-3-343

Mesinger F, Janjic ZI (1974) Noise due to time-dependent boundary conditions in limited area models. GARP Programme Numer Exp Rep 4:31–32

Milanovic PT (1981) Karst hydrology. Water Resources Publications, Highlands Ranch, 434 pp

Mitchell K (2005) The community Noah land surface model (LSM)—user's guide public release version 2.7.1. ftp://ftp.emc.ncep.noaa.gov/mmb/gcp/ldas/noahlsm/ver_2.7.1. Last visited 12 Sept 2014

Mlawer EJ, Taubman SJ, Brwon PD, Iacono MJ, Clough SA (1997) Radiative transfer for inhomogeneous atmosphere; RRTM, a validated correlated-k model for the longwave. J Geophys Res 102(D14):16 663–16 682

Moser BK, Stevens GR, Watts CL (1989) The two-sample t-test versus Satterwaite's approximate F test. Commun Stat Theory Methodol 18:3963–75

Oke TR (1987) Boundary layer climates, 2nd edn. Routledge, London, pp 110–157

Palmer AN (2007) Cave geology. Cave Books, Dayton, 454 pp

Petty GW (2008) A first course in atmospheric thermodynamics. Sundog Publishing, Madison, 337 pp

Pielke RA (2001) Influence of the spatial distribution of vegetation and soils on the prediction of cumulus convective rainfall. Rev Geophys 39(2):151–177

Quintanar AI, Mahmood R (2012) Ensemble forecast spread induced by soil moisture changes over mid-south and neighbouring mid-western region of the USA. Tellus A Dyn Meteorol Oceanogr 64:17156. doi:10.3402/tellusa.v64i0.17156

Quintanar AI, Mahmood R, Loughrin J, Lovanh NC (2008) A coupled MM5-Noah land surface model-based assessment of sensitivity of planetary boundary later variables to anomalous soil moisture conditions. Phys Geogr 29:54–78. doi:10.2747/0272-3646.29.1.54

Quintanar AI, Mahmood R, Motley MV, Yan J, Loughrin J, Lovanh N (2009) Simulation of boundary layer trajectory dispersion sensitivity to soil moisture conditions: MM5 and Noah-based investigation. Atmos Environ 43:3774–3785

Rodell M, Houser PR, Berg AA, Famigliett JS (2005) Evaluation of 10 methods for initializing a land surface model. J Hydrometeorol 6(2):146–155

Ruxton GD (2006) The unequal variance t-test is an underused alternative to Student's t-test and the Mann–Whitney U test. Behav Ecol 17(4):688–690. doi:10.1093/beheco/ark016

Santanello JA Jr, Kumar SV, Peters-Lidard CD, Harrison K, Zhou S (2013) Impact of land model calibration on coupled land-atmosphere prediction. J Hydrometeorol 14(5):1373–1400

Schwinning S (2008) The water relations of two evergreen tree species in a karst savanna. Oecologia 158(3):373–83

Skamarock WC, Klemp JB, Dudhia J, Gill DO, Barker DM, Duda MG, Huang XY, Wang W, Powers JG (2008) A description of the advanced research WRF version 3. NCAR tech note, NCAR/TN-475+STR

Suarez A, Mahmood R, Quintanar AI, Beltran-Przekurat A, Pielke RA Sr (2014) A comparison of the MM5 and the Regional Atmospheric Modeling System simulations for land–atmosphere interactions under varying soil moisture. Tellus A Dyn Meteorol Oceanogr 66:21486. doi:10.3402/tellusa.v66.21486

Weary DJ, Doctor DH (2014) Karst in the United States: a digital map compilation and database. US geological survey open-file report, pp 2014–1156

White WB (1988) Geomorphology and hydrology of karst terrains. Oxford University Press, New York, 480 pp

White WB, Culver DC, Herman JS, Kane TC, Mylroie JE (1995) Karst lands. Am Sci 83:450–459

Wilks DS (2010) Statistical methods in the atmospheric sciences, 3rd edn. Academic Press, New York, 676 pp

Winchester J, Mahmood R, Rodgers W, Hossain F, Rappin E, Durkee J, Chronis T (2017) A model-based assessment of potential impacts of man-made reservoirs on precipitation. Earth Interact 21:1–31

Xue Y, Sellers PJ, Kinter JL, Shukla J (1991) A simplified biosphere model for global climate studies. J Clim 4:345–64

Zhang Q, Xu CY, Zhang Z, Chen X, Han Z (2010) Precipitation extremes in a karst region: a case study in the Guizhou province, southwest China. Theor Appl Climatol 101:53–65. doi:10.1007/s00704-009-0203-0